Separation and Purification Technology 409 (2026) 139242

Contents lists available at ScienceDirect

Separation and Purification Technology

journal homepage: www.elsevier.com/locate/seppur

A novel fractional crystalisation-based method for the purification of tellurium to 5 N purity

Hanwen Chung, Semiramis Friedrich *, Bernd Friedrich

IME Process Metallurgy and Metal Recycling, RWTH Aachen University, 52072 Aachen, Germany

ARTICLE INFO

Editor: Dr. B. Van der Bruggen

Keywords:
Tellurium
Fractional crystallisation
High purity
Cooled finger

ABSTRACT

The purification of Tellurium to ultra-high purity levels using multi-pass zone melting remains as state-of-the art method, but it is very time-intensive as slow and repeated processing are required. In this study, a rotational Cooled Finger crystallisation approach is investigated as a pre-purification step to accelerate the purification process prior to zone melting. A systematic experimental study was conducted using 4 N (99.99%) tellurium as feed material, examining the combined effects of rotation rate (25–200 RPM) and cooling gas flow rate (20–120 L/min) on refining performance. Under favourable conditions, the Cooled Finger process achieved purification to 5 N (99.999%) within a single crystallisation step of 30 min. Total impurity concentrations were reduced from 100 ppm to ranges of 5-60 ppm, corresponding to refining efficiencies of 42–90%, with material yields ranging from 8% to 25%. The results show that the refining performance is governed by the interplay between solidification dynamics, temperature gradient and solute transport, which are collectively controlled by the applied rotation and cooling conditions. Compared to conventional zone melting, the Cooled Finger process provides significantly faster impurity reduction. Using it as a supplementary method to zone melting substantially lowers the impurity burden, and may reduce overall processing time required for achieving ultra-high purity tellurium.

1. Introduction

Tellurium is a metalloid commonly produced as a by-product of copper anode sludge processing and has found applications across several industrial sectors. In metallurgy, tellurium is used as an additive to enhance the mechanical properties of steel [1,2]. In the chemical industries, tellurium chlorides are employed in metal coating processes and as catalyst for the synthetic fibre production. Tellurium is also used in glass and ceramics to provide blue to brown colours. The largest share of tellurium application, however, is associated with advanced functional materials, particularly photovoltaic solar cells in the form of CdTe and thermoelectric materials based on Bi_2Te_3 alloyed with either Sb (P-type) or Se (N-Type) [3].

In the area of applications in solar cells and thermoelectric materials, the use of high-purity tellurium as a starting material is crucial for the development of II-VI semiconductor compounds, as elevated impurities content can significantly affect the dopant incorporation and electrical performance. The required purity of starting materials for manufacturing process of such products is typically 5 N (99.999%) or higher, with increasing demand for purities approaching 6 N (99.9999%) as material performance requirements continue to rise.

Several purification routes have been investigated to achieve ultra-high-purity tellurium. As demonstrated in laboratory experiments, the process of vacuum distillation has been shown to purify tellurium to purities approaching 6 N [4,5]. However, this technique is not employed industrially for the production of such high purity tellurium, likely due to operation difficulty and limited process efficiency. At present, the most advanced and widely adopted industrial processing technique is zone melting, a fractional crystallisation-based process originally introduced by Pfann [6] in 1952. This method has demonstrated the capability to produce tellurium with ultra-high purity; however, it is inherently time-intensive. Shim et al. [7] reported that purification of 4 N tellurium under hydrogen atmosphere required approximately 26.5 h to reduce Bi from 5 ppm, Sb from 25 ppm, and Sn from 20 ppm to below detection limits, and to decrease Se content from 50 ppm to 0.56 ppm. Zaiour et al. [8] combined multi-zone melting and distillation to produce 7 N tellurium, with the cumulative time for the three-zone melting stage amounting to approximately 10.5 h. Tian et al. [9] refined 400 g of 4 N tellurium to 5 N7 after nine passes of multi-zone melting, achieving impurity removal of 89.49% over a total processing time of

* Corresponding author.
E-mail address: sfriedrich@ime-aachen.de (S. Friedrich).

https://doi.org/10.1016/j.seppur.2026.139242
Received 11 May 2026; Received in revised form 23 June 2026; Accepted 5 July 2026
Available online 6 July 2026

approximately 35.5 h. Numerous other studies have reported similar trends, where ultra-high purity is achieved at the expenses of extended processing durations [10–13].

Industrial production of high-purity tellurium follows the same general pattern, requiring multiple zone-melting passes and long cumulative processing times [14]. From an industrial perspective, where process efficiency, throughput, and operating cost control are critical, the prolonged processing times associated with zone melting present a clear demand for improvement. In this context, alternative or supplementary fractional crystallisation techniques that can reduce the impurity burden prior to zone melting are of particular interest.

One such technique originates from a process developed by Showa Aluminium Corporation for the production of high purity aluminium [15]. The process employs an immersed rotation cooling body to promote controlled crystallisation of high-purity metal on the surface of the body. Subsequent modifications of this concept have led to what is now referred to as the "Cooled Finger" process, which has been reported over the past decade for the purification of several metals, including aluminium [16], magnesium [17] and germanium [18]. Rather than being proposed as a replacement for zone melting, the Cooled Finger process offers potential as a supplementary pre-purification step, enabling early-stage impurity rejection and thereby reducing the number of subsequent zone-melting passes required to achieve ultra-high purity.

Similar to zone melting, the Cooled Finger process operates on the principle of fractional crystallisation, which relies on difference in solubility of impurities between the solid and molten phases of a metal [13,19]. The purification behaviour is commonly characterised using a distribution coefficient, k_0, defined under isothermal and isobaric equilibrium solidification conditions, as shown in eq. (1).

$$k_0 = \frac{C_s}{C_L}$$

C_i : Concentration of element in the $(i = S)$ solid phase, $(i = L)$ liquid phase (1)

The distribution coefficient represents the theoretically achievable extent of impurity segregation in a binary system, assuming complete diffusion of rejected solute into the liquid phase. For a given system, the value of k_0 may be less than or greater than unity. Impurities with $k_0 < 1$ exhibit limited solubility in the solid phase and are preferentially rejected into the melt, whereas impurities with $k > 1$ tend to concentrate in the solid, rendering their removal by fractional crystallisation more challenging. It should be noted that distribution coefficients depend on both equilibrium temperature and impurity concentration range, as illustrated schematically in Fig. 1.

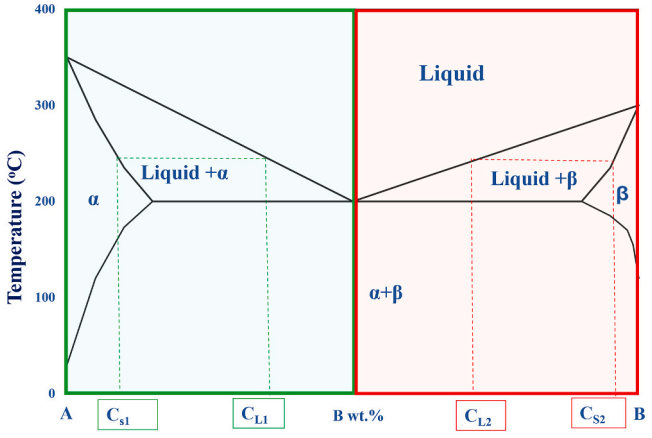

Fig. 1. Eutectic binary diagram with k < 1 when B is <50 wt% (green area) and k > 1 when B > 50 wt. (red area). (For interpretation of the references to colour in this figure legend, the reader is referred to the web version of this article.)

In practice, equilibrium solidification conditions are rarely achieved during metal purification. To account for non-equilibrium effects, Burton, Prim, and Slichter (BPS model) [20] proposed a more realistic model incorporating the influence of a hypothetical diffusion boundary layer thickness δ, the growth rate of the solid phase V, and the diffusion coefficient of the elements in the matrix D. The resulting effective distribution coefficient, k_{eff}, is expressed in eq. (2).

$$k_{eff} = \frac{k_0}{k_0 + (1 - k_0) \bullet \exp\left(-\frac{V\delta}{D}\right)} \tag{2}$$

Within this framework, the hypothetical boundary layer thickness ($\delta \approx 1.6 \bullet D^{\frac{1}{3}} \bullet \nu^{\frac{1}{6}} \bullet \omega^{-\frac{1}{2}}$) depends on the angular velocity of crystal rotation ω (in s^{-1}), kinematic viscosity of melt ν (in m^2s^{-1}), as well as the diffusion coefficient of impurity in the melt D (in m^2s^{-1}).

For the Cooled Finger process, the rotation rate (ω_{CF}) is directly controlled through the rotation of the motor attached to the cooling body (in revolutions per minute), while the growth rate is influenced by the applied cooling gas flow rate (Q_g). Curtolo et al. [21] experimentally demonstrated the influence of both parameters on impurity removal during aluminium purification. Lower cooling rates resulted in improved purification efficiency due to reduced growth velocity, whereas excessively low growth rates promoted temperature homogenization and potentially back-melting [22]. Increasing ω_{CF} enhanced impurity rejection up to an optimal limit, beyond which excessive turbulence at the solidification front led to boundary layer instability, non-uniform growth, and partial re-melting.

For tellurium, experimentally determined distribution coefficients (k_{exp}) obtained from various fractional crystallisation processes has been compiled in Table 1. The majority of reported k_{exp}values are below unity, suggesting that most impurities should, in principle, be removable by fractional crystallisation. Unlike aluminium or magnesium systems, equilibrium distribution coefficients for tellurium could not be calculated e.g. using Factsage ™ thermodynamic modelling software due to the limited availability of reliable binary Te-X databases. This limitation arises primarily from the extremely low solubility of many elements in high-purity tellurium, resulting in solid-phase regions that are too narrow to be resolved in conventional phase diagrams. Despite this, several impurities, including Fe, Ni, Pb, and Bi could be more difficult to be removed by fractional crystallisation, potentially due to the possible local formation of heavy molecules in tellurium like Fe_2Te_3, Ni_2Te_3, PbTe, Bi_2Te_3 and Cu_2Te [23].

Other than solubility, the efficiency of impurity removal during fractional crystallisation is also strongly influenced by the solidification morphology [22]. Planar solidification is generally considered the most favourable regime for purification, as solute elements are rejected uniformly into the liquid phase and redistributed ahead of the advancing solidification front. In contrast dendritic growth can promote solute entrapment within intercellular or inter-dendritic regions, reducing the effectiveness of impurity separation [26]. The stability of the solidification front is governed by the balance between the temperature gradient at the solid-liquid interface and the solidification front velocity (compare Fig. 2), both of which are controlled indirectly by processing conditions. In the Cooled Finger process, these parameters are influenced by Q_g and ω_{CF}, motivating the characterisation of temperature gradients and solidification front velocity in order to assess the attainable solidification regimes and their implications for purification efficiency.

Previous investigations by the authors [25] have indicated that the Cooled Finger process may offer promising impurity separation behaviour in tellurium systems. However, a systematic evaluation of impurity distribution behaviour, process parameters effects, and purification limits for tellurium using this method remained lacking. Recent studies have demonstrated the feasibility of rotational and immersed crystallisation processes for the purification of tellurium, achieving high

Table 1
Experimental determined distribution coefficient of Te, adapted from [1,13,24,25].

Element	k_{exp}	Element	k_{exp}
Ag	0.08, 0.086	Mn	0.03, 0.08,0.1,0.2
Al	0.07, 0.19, 0.16, 0.14, 0.58[25],0.96[25]	Mo	0.16
As	0.1, 0.031, 0.04,0.12, 0.72	Na	0.06, 0.67
Bi	0.5, 0.83, 0.92	Ni	0.04,0.58,0.39,0.82
Ca	0.01, 0.28	Pb	0.19, 0.02, 0.096
Cd	0.26	S	0.29
Cr	0.05, 0.24, 0.25	Sb	0.35
Cu	0.005, 0.011, 0.23, 0.32, 0.58	Se	0.44, 0.48, 0.58
Fe	0.02, 0.05, 0.26	Si	0.15
Hg	0.14	Sn	0.22
In	0.009, 2.82	Ti	0.004
Mg	0.093, 0.1	V	0.06
		Zn	0.028, 0.25, 0.91

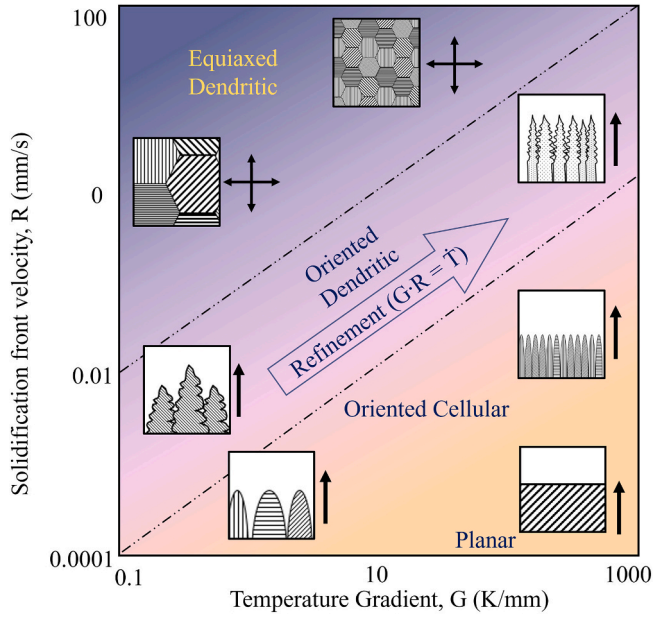

Fig. 2. Solidification morphologies depending on solidification rate R (mm/s) and temperature gradient G /K/mm), with the black arrows representing growth direction. (reproduced from [26]).

impurity removal efficiencies and significantly reduced processing times compared to conventional zone melting [19,27]. In one implementation, rotation of the furnace or entire melt is required, introducing additional mechanical and thermal complexity that may limit industrial scalability [27]. Although the yield is not explicitly reported, the published data indicate that only 1-16 g of purified metal were obtained from 3 to 6 kg of feed material, suggesting a very low overall recovery. The other one have primarily focused on demonstrating impurity removal potential, while providing limited analysis of process configuration, yield, and the effect of controllable parameters such as cooling body rotation rate and cooling gas flow rate [19]. The overall refining efficiencies of approximately 75–80% under their respective operating conditions were reported. However, direct quantitative comparison between different crystallisation systems remains difficult due to variations in feed composition, process configuration and performance metrics. Consequently, a systematic evaluation of a mechanically simplified Cooled Finger for tellurium, with quantitative determination of impurity distribution coefficients and mapping of process parameter, remains lacking.

The present study therefore aims to investigate the purification of tellurium using the Cooled Finger process, with particular emphasis on determining experimental distribution coefficients k_{exp} for several impurities, including As, Fe, Ni, Pb, Se and Zn. These elements were selected due to their frequent occurrence in tellurium derived from copper anode sludge, where they coexist with more commonly studied elements such as Cu, Bi, Sb, Ag and Sn. While the segregation behaviour of Cu, Bi, Sb and Sn during tellurium purification has been extensively reported in the literature, comparatively limited data are available for As, Ni, Fe, and Zn under fractional crystallisation. The influence of cooling body rotation rate and cooling gas flow rate on purification efficiency is examined in detail, and the operational limits of the process, including growth stability and yield considerations, are discussed. Rather than proposing the Cooled Finger as a replacement for zone melting, this work explores its potential role as a supplementary pre-purification step capable of reducing the overall processing time required to achieve ultra-high-purity tellurium.

2. Experimental methods

The Cooled Finger assembly consisted of a hollow steel shaft connected to a motor, with an ET-10-graphite shell attached at its lower end. The hollow shaft allowed cooling gas to flow internally, thereby cooling the steel shaft, consequently the graphite shell and the surrounding molten tellurium upon immersion. A schematic illustration of the experimental setup, installed in a resistance heated furnace, is shown in Fig. 3.

A series of 25 experimental trials were conducted to investigate the purification tellurium using the Cooled Finger method. The key controlled parameters were the rotation rate, ω_{CF} (in revolutions per minute, RPM) and the cooling gas flow rate, Q_g (in L/min). The selected parameter ranges (25–200 RPM and 20–120 L/min) were defined based on a combination of literature data, previous trials, and operational constraints of the experimental setup. Previous studies on tellurium systems have investigated ranges from 0 to 120 RPM at 10 L/min [27], and 200/400 RPM without indication of cooling condition [19]; however, in the present work, the parameter window was extended to cover a broader range of operating conditions. In addition, studies on comparable purification systems for metals such as Al [22] and Mg [17] report rotation rates and cooling conditions within a similar order of magnitude, supporting the physical relevance of the selected ranges. The experiments were conducted at five different rotation rates (25, 50, 80, 120 and 200 RPM) and five different cooling gas flow rates (20, 40, 60, 100, 120 L/min). A detailed list of all experimental conditions is provided in Table 2.

Due to the tendency of tellurium to volatilise at temperatures well below its boiling point [28], the experiments were not conducted in an open system. Instead, all experiments were carried out in an enclosed system continuously flooded with Ar gas to provide an inert atmosphere free from oxidation of the metal, with the entire setup connected to an off-gas suction system. For each experiment, approximately 6–6.5 kg of tellurium with a purity of 99.99 wt% (Wuhan Tuocai Technology Co., Ltd., China, exemplary chemical composition in Table 3) was charged

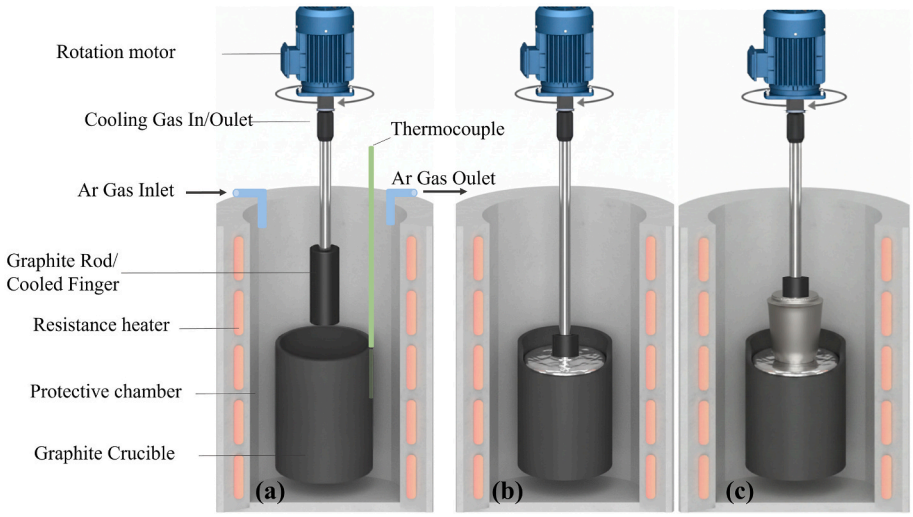

Fig. 3. Illustration of experimental setup for the cooled finger process: (a) schematic representation of the apparatus; (b) experimental configuration with the cooling body submerged during crystallisation; and (c) configuration after completion of crystallisation and withdrawal of the cooling body.

Table 2
List of experiments and parameters.

Test	Rotation rate, ω_{CF} [RPM]	Cooling gas flow rate, Q_g[L/min]
1	25	20
2	25	40
3	25	60
4	25	100
5	25	120
6	50	20
7	50	40
8	50	60
9	50	100
10	50	120
11	80	20
12	80	40
13	80	60
14	80	100
15	80	120
16	120	20
17	120	40
18	120	60
19	120	100
20	120	120
21	200	20
22	200	40
23	200	60
24	200	100
25	200	120

Table 3
Chemical composition of the as-purchased tellurium as provided by the manufacturer (in ppm).

Cu	Mg	Bi	Fe	Na	As	Al	Se	Pb
8.733	0.1	1.025	7.79	18.91	0.1	0.1	11.126	0.1

into the crucible in the form of solid chunks. The amount of tellurium was selected such that the molten metal reached approximately 70% of the crucible height, ensuring safe operation and preventing overflow during submersion and rotation.

The crucible was initially heated to 550 °C, i.e. almost 150 °C higher than the liquidus temperature of pure Tellurium, to ensure rapid and complete melting of the tellurium charge. After melting, the temperature was reduced and stabilized at approximately 5–10 °C above the melting point. Once the melt was fully molten, an initial melt sample was collected for the starting impurity concentrations (C_0). Since impurity concentrations in the ppm range can significantly influence the experimental results, a separate analysis was performed instead of relying on the supplier provided nominal composition. Following sampling, the system was held undisturbed for 5 min to allow thermal homogenization of the melt.

Prior to submersion, the Cooled Finger was positioned inside the furnace above the melt, such that it was preheated together with the crucible and the tellurium material inside. This approach minimized rapid solidification during immersion. The Cooled Finger was then submerged into the molten tellurium roughly 5-7 cm above the bottom of the crucible. Rotational speed and cooling gas flow were initiated almost immediately to start crystallisation.

Crystallisation occurred on the surface of the graphite shell through fractional crystallisation under forced cooling from the steel shaft and rotation shear. Each crystallisation run was conducted for a fixed duration of 30 min ± 30s. This processing time was selected as a compromise between purification efficiency and melt contamination, as prolonged operation leads to impurity enrichment in the residual liquid phase and a corresponding decrease in purification efficiency.

At the end of the crystallisation period, rotation was stopped first, followed by the withdrawal of the Cooled Finger from the melt. Cooling gas flow was maintained during withdrawal to prevent re-melting of the crystallised tellurium. The remaining tellurium was left molten and a residual melt sample (C_L) was collected immediately after removal of the Cooled Finger. After cooling to room temperature under argon atmosphere, the crystallised tellurium was mechanically detached from the graphite shell. A solid product sample (C_s) was taken from the crystallised tellurium. Although the graphite shell is theoretically reusable, a new one was used for each experiment in order to eliminate any risk of cross-contamination between runs. The mass of the crystallised tellurium was measured and the process yield was calculated by comparing the mass of crystallised tellurium to the initial mass of tellurium charged into the crucible. All collected samples (C_0, C_L, and C_S) were analysed using inductively coupled plasma mass spectrometry (ICP-MS, Agilent 7850, Agilent Technologies, California USA). To ensure reliability, all measurements were conducted in duplicates for each experimental trial. Experimental distribution coefficients (k_{exp}) and purification efficiencies (η_r) were calculated based on the measurement results. The growth rate (V_{CF}) of tellurium during Cooled Finger crystallisation was determined by dividing the average thickness of the solidified material by the fixed crystallisation time of 30 min. Yield of the Cooled Finger was calculated using the mass ratio of refine tellurium to input tellurium.

$$k_{exp,(i)} = \frac{C_{s,i}}{C_{L,i}}$$

$C_{s,i}$: concentration of i = As, Fe, Ni, Pb, Se and Zn in the crystallised phase
$C_{L,i}$: concentration of i = As, Fe, Ni, Pb, Se and Zn in the remaining melt

(3)

$$\eta_r = \left(1 - \frac{\sum C_{s,i}}{\sum C_{0,i}}\right) * 100\%$$

$C_{0,i}$: concentration of i = As, Fe, Ni, Pb, Se and Zn in the initial melt

(4)

$$V_{CF} = \frac{d_{avg}}{t_{crys}}$$

d_{avg} : average thickness of solidified layer;
t_{crys} is the crystallisation time

(5)

$$Y = \frac{m_{CF}}{m_0} * 100\%$$

m_{CF} : mass of refined Te;
m_0 is the mass of input material

(6)

The three-dimensional results from the yield, growth rates, purification efficiencies and distribution coefficients presented in the following section were constructed from the 25 experimentally measured parameter combination. For visualization purpose, the discrete data were interpolated using the XYZ gridding function in OriginPro 2023 onto a 30 × 30 matrix employing bicubic convolution algorithm. The resulting surface plots of the results therefore do not represent additional experimental measurements or fitted models.

Additionally, two separate experiments for temperature gradient G measurements were performed for a representative cooling gas flow rate of 60 L/min, selected as an intermediate operating condition within the investigated parameter range. The objective of these measurements was to characterise the solidification regime established under the Cooled Finger process and to assess the proximity of the process conditions to a planar solidification, rather than to conduct a full parametric study of temperature gradients. Consequently, it provided insight into potential design modifications of the Cooled Finger required to access different solidification regimes in future process development.

Temperature data were recorded continuously from the onset of crystallisation until the end of crystallisation period, including the withdrawal of the submerged Cooled Finger. Two Type-K thermocouple were fixed relative to the graphite shell at horizontal or vertical positions (compare Fig. 4). The thermocouple and the Cooled Finger remained stationary during the experiment i.e. without rotation. The error of the measurements is ±0.005 K, and no thermocouple lag was detected under the experimental conditions. The temperature gradients G_{ver} and G_{hor} were calculated by taking the temperature difference over the distance between the thermocouple.

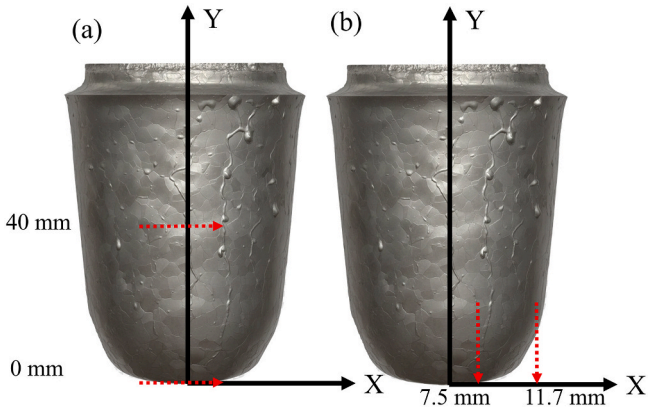

Fig. 4. Positions of the thermocouples within the solidified tellurium crystal used for temperature gradient measurements, (a) vertical temperature measurement at $Y = 0$ mm and $Y = 40$ mm; (b) horizontal temperature measurement at $Y = 0$ mm between positions $X_1 = 7.5$ mm and $X_2 = 11.7$ mm relative to the cooled finger.

3. Results and discussion

Temperature-time profiles recorded during solidification exhibited a reproducible course consisting of an initial cooling stage followed by a stable crystallisation period. Fig. 5 shows five representative temperature-time curve obtained at different cooling gas flow rates, Q_g. For all investigated rotation rates, ω_{CF}, the overall shape of the temperature-time curves remained unchanged with no transient behaviour observed, indicating that ω_{CF}did not significantly influence the thermal field under the present conditions. In contrast, variations in Q_g primarily influence the cooling rate of the melt, requiring higher immersion temperature with increasing Q_g to maintain stable near crystallisation. During the main solidification interval, corresponding to the quasi-plateau regions in the temperature-time profiles, only minor temperature fluctuations were observed, with a total temperature decrease of less than 1 K. This behaviour indicates that quasi-steady thermal conditions were maintained over most of the solidification period, supporting the use of averaged growth rates measured by taking the thickness of the solidified metal over total time as solidification front velocities, and averaged temperature gradients in the subsequent analysis.

3.1. Yield and growth rate

Since the growth rate (V_{CF}) was determined by dividing the average thickness by crystallisation time, the reported values therefore represent an average V_{CF} over the full crystallisation period instead of transient variations. Fig. 6(a) shows the combined influence of the cooling gas flow rate, Q_g and rotation rate, ω_{CF} on the measured V_{CF}. Over the investigated range, V_{CF} increased monotonically with increasing Q_g from 20 to 80 L/min. At higher Q_g (100–120 L/min), the increase in V_{CF} became less pronounced, indicating a diminishing sensitivity to further increases in cooling intensity. Here, the cooling capacity approaches a limit where further heat transfer becomes restricted by the thermal conduction between the steel shaft and graphite shell.

Rotation of the Cooled Finger introduced a secondary modulation of V_{CF}. For a given Q_g, changes in the Cooled-Finger rotational velocity, ω_{CF} resulted in only minor variations in the measured growth rate with no abrupt transitions across the investigated parameters space. This indicates that, within the present operating window, the growth rate is

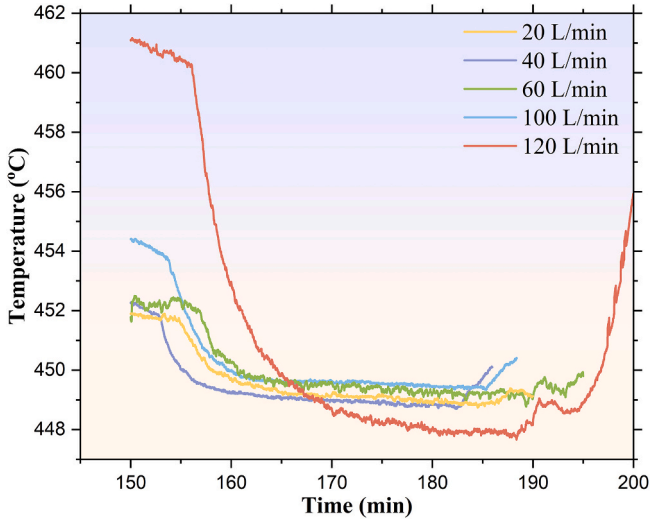

Fig. 5. Selected temperature-time profile during Cooled Finger crystallisation.

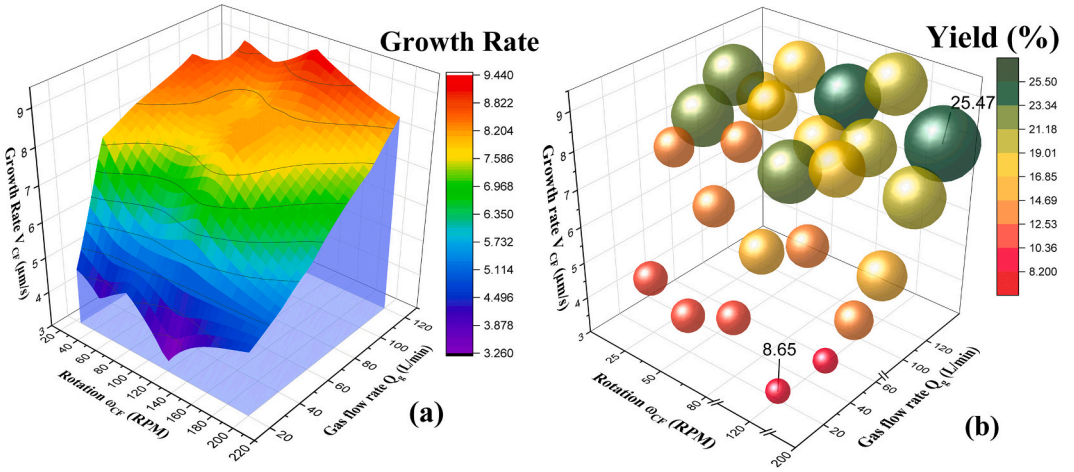

Fig. 6. Process parameter map showing the dependence of tellurium growth rate on ω_{CF} and Q_g during Cooled Finger crystallisation: (a) three-dimensional colour map of growth rate; (b) corresponding bubble plot, where bubble's size represents the crystallised yield (%).

primarily by the cooling intensity, while rotation plays a subordinate role.

To further visualise the material yield, the same dataset is presented in Fig. 6(b) using a bubble representation, where the bubble size corresponds to the material yield, defined as the ratio of collected solidified mass to the initial charge.

At low Q_g (20 and 40 L/min), weak cooling intensity slows down crystallisation and thereby results in lower yield, with a barely decreasing yield with increasing ω_{CF}. From yield perspective, this effect is unfavourable; however, the associated improvement in purification efficiency is of equal relevance and therefore should be considered in parallel (Section 3.2). At an intermediate Q_g of 60 L/min, the collected mass showed no clear dependence on ω_{CF}, while at higher Q_g (100 and 120 L/min), increasing ω_{CF} only resulted in a marginally higher collected mass. This suggest that, under sufficient cooling conditions, solidification is predominantly governed by heat transfer, and the effect of rotation remains secondary. The slight variations observed with increasing ω_{CF} can be attributed to hydrodynamic effects such as shear at the solid-liquid interface and modifications of local cooling conditions, which may influence crystal attachment and growth kinetics, but do not significantly alter the overall yield.

Compared to previously reported rotation crystallisation of tellurium, which reported a highest yield of 0.9% (27 g from 3 kg input feed), the present work achieves significantly higher material recovery, with yields ranging from 8.6% to 25.4%. It is worth noting that the obtained yields are comparable to those reported for aluminium and magnesium using similar Cooled Finger setup from the same laboratory, where average yields are approximately 13% with a maximum of approximately 30%. This suggests that the observed yield is primarily governed by the characteristic of the setup rather than being solely material-specific. In this context, the yield is consistent with the process behaviour, and further increases can be expected with extended crystallisation time.

3.2. Purification efficiencies and K-values of selected impurities

The implications of the above growth behaviour for impurity rejection are reflected in the purification efficiency, η_r, shown in Fig. 7. The η_r obtained across all investigated conditions ranged from 42.2% to 90.4%. All refined samples exceeded 4 N5 purity (< 50 ppm total impurities), demonstrating stable purification performance across the investigated operating window, even when optimal conditions are not met.

A clear dependence of η_r on ω_{CF} was observed. At low ω_{CF} (25 and 50 RPM), refining efficiencies remained consistently low and showed limited sensitivity to Q_g. Increasing ω_{CF} to 80 RPM resulted in a clear

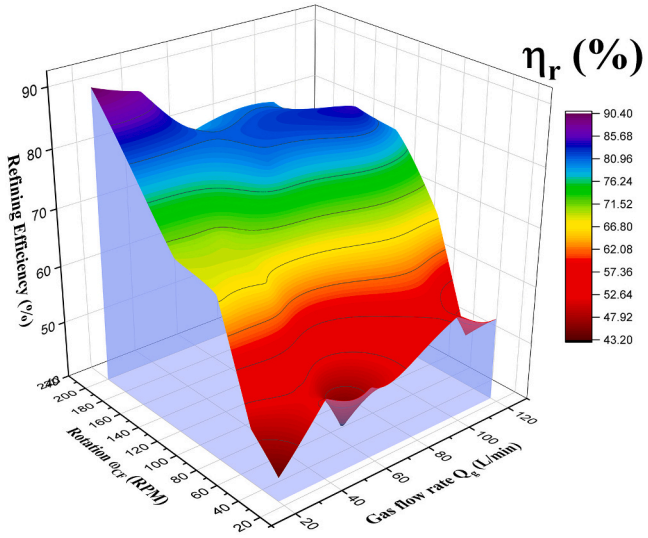

Fig. 7. Purification efficiency of all impurities in tellurium as a function of rotation rate and cooling gas flow rate during Cooled Finger refining.

improvement in η_r, while further increase to 120 and 200 RPM led to substantially higher values. All samples reaching 5 N purity were obtained at high ω_{CF} (200 RPM at 20 L/min and 200 RPM at 40 L/min), with lower Q_g consistently resulted in higher η_r. The overall contribution of $Q_g$to the variation in purification efficiency remained limited, typically accounting for less than 15% differences across the investigated range. At high ω_{CF} (120–200 RPM) combined with high Q_g (100–120 L/min), purification efficiency tended to decrease slightly, despite these conditions yielding with 25.47% the largest collected metal (compare Fig. 6(b)).

The highest η_r were observed under combined of high ω_{CF} and low Q_g conditions, since lower Q_g promotes slower solidification, allowing more time for solute rejection and redistribution. Although reduced cooling intensity may decrease temperature gradient, previous G_{hor} measurements indicate that the system remains within the cellular solidification regime, such that moderate reductions do not induce dendritic instability, and instead support improved purification performance through kinetic effects.

Several conditions yielded products close to, but not exceeding the 5 N purity threshold e.g. 11–20 ppm of total impurities corresponding to 4 N8-4 N89 for tests at 120 RPM. To provide quantitative context for the

purification performance, Table 4 summarises the initial and final impurity concentrations for four representative samples. These include two conditions achieving 5 N purity (1 and 2), one condition corresponding to the lowest purification efficiency (3), and one near-threshold case at 4 N85 purity (4). These near-threshold cases are attributed to minor variations in trace impurity concentrations at the sub-ppm level, where small absolute differences can lead to relatively large changes in calculated purification efficiency. Such fluctuations are inherent to high-purity purification and do not indicate a fundamental limitation of the process. Overall, these results demonstrate that substantial impurity rejection can be achieved within a short crystallisation time (~30 min). Further optimisation, particularly through improved thermal control or extended solidification times, may enable even higher and more consistent purity levels.

The measured initial impurity concentrations of the melts differed slightly from the values from the raw material composition in Table 3. This discrepancy may be attributed to batch-to-batch variations in the raw materials, possible volatilization or redistribution of impurities during melting, and sampling uncertainty. Therefore, the experimentally measured impurity concentrations were used as the initial values for all analyses and calculations.

The experimental distribution coefficients k_{exp} of the investigated impurity elements Fig. 8 exhibit clear but element-dependent trends as a function of ω_{CF} and Q_g. Although it was mentioned that increasing rotation generally promotes solute rejection, the response of individual elements is non-monotonic, likely due to the differences in element-specific diffusion coefficient as well as chemical reactivity and interactions with other elements.

Selenium exhibits two maxima in k_{exp} at low rotation (25 RPM) combined with both lowest (20 L/min) and highest (120 L/min) Q_g. Between 40 and 100 L/min, k_{exp} decreases smoothly with increasing ω_{CF}, from approximately 0.6 to 0.25, indicating progressively enhanced segregation. Arsenic shows a similar result, with elevated k_{exp} values at low rotation (40 RPM) and low or high cooling gas flow rates, followed by a gradual decrease at higher rotation rate, spanning 0.4 to 0.15. Lead follows the same general trend, with k_{exp} values in the range 0.15 to 0.5, suggesting comparable segregation behaviour among these elements.

Nickel displays a distinctly different behaviour, where although there are two pronounced maxima in k_{exp} at 25 RPM for both 20 and 120 L/min, the remaining conditions resulted in a broad plateau with limited sensitivity to either ω_{CF} or Q_g. Across the investigated parameters, k_{exp} for Ni remains within 0.04–0.2 excluding the two maxima, indicating a weaker dependence on process parameters compared to Se, As, and Pb. Zinc shows only weak sensitivity to both $\omega_{CF}$and Q_g, with k_{exp} remaining in the range of 0.16 to 0.30, except for a single maximum at 40 RPM, 120 L/min. Iron exhibits the most pronounced ω_{CF} dependence. Between 25 and 80 RPM, k_{exp} remains around 0.31 to 0.37 for all Q_g except 120 L/min. At 120–200 RPM, a consistent decrease in k_{exp} is observed across all Q_g, reaching values as low as 0.129 (200 RPM at 20 L/min).

The differing behaviour of Fe and Zn may reflect mutual interaction effects commonly reported for these elements in metallic systems (e.g. Γ-Fe_3Zn_{10}, δ_k-$FeZn_7$, or ζ-$FeZn_{13}$), potentially influence diffusion behaviour and local solute re-distribution even at trace concentrations. This further applies to the mentioned system of Fe—Te, Ni—Te and Pb—Te, representing one possible explanation for the observed local maxima in the distribution coefficients. While the formation of intermetallic phases cannot be confirmed under the present conditions, such interactions may contribute to the observed deviations form monotonic behaviour.

The formation of intermetallic compounds generally requires local enrichment of impurity species, sufficient undercooling, and adequate time for nucleation and growth. At lower ω_{CF}, reduced melt convection leads to the development of solute accumulation at the interface. Simultaneously, higher Q_g enhance heat extraction, increasing the degree of local undercooling and could theoretically favour local phase interactions if such phases were thermodynamically stable under the investigated conditions.

However, the increased incorporation of elements such as Se and As at low rotation rates cannot be attributed to intermetallic formation like the other elements, but is more likely governed by mass transport limitations in a local multi-component system. The mass transport limitation may also apply to the other elements, as impurity clusters, intermetallic compounds and individual elements may accumulate, limiting diffusion between the interfacial region and the bulk melt. Such interactions between elements can modify their effective thermodynamic behaviour, including changes in activity, partitioning tendencies, and interfacial properties.

It should be noted that the investigated impurity concentrations are in the ppm range, and the calculated values are therefore based on very small absolute differences in concentration. As a result, even minor variations in measured values can lead to relatively large changes in the calculated coefficients. For example, a change from 1 ppm to 0.6 ppm at a given reference concentration corresponds to a significant relative difference, although the absolute variation remains minimal. This inherently high sensitivity must be considered when interpreting fluctuations in the distribution coefficients. The average deviation was found to be within ±0.05 ppm, indicating a high level of analytical precision and confirms that the observed trends are reproducible within the limits of measurement uncertainty.

Although the calculated k_{exp} ranges are relatively broad compared to the values in Table 1, this variation arises primarily from two factors. First, the investigated impurity concentrations are at trace levels, where small absolute deviations in ppm can translate into comparatively large changes in calculated distribution coefficients. Second, the experiments were conducted over a wide operational window encompassing significantly different rotational speeds and cooling intensities, which intentionally produces strong variations in solute transport conditions.

Overall, the results indicate that rotation rate is the dominant parameter governing impurity segregation, while Q_g plays a secondary role that becomes relevant primarily at higher ω_{CF}. Most reported tellurium purification studies quantify impurity removal on an element-specific basis, typically though multi-pass zone melting. Processes that are more directly comparable to the present Cooled Finger approach have been reported to exhibit very low yield of 0.5% - 1%, and limited product purity with total impurities of 13.08 ppm from 52.23 ppm,

Table 4
Initial and final impurity concentrations (ppm) of representative samples illustrating the purification performance under selected processing conditions (DL: detection limit).

Samples and parameters		Na	Al	Cr	Mn	Fe	Ni	Cu	Zn	As	Se	Pb	Sum
200 RPM, 20 L/min	Final	0.03	0.98	0.19	0.08	1.97	0.26	<dl	1.36	0.02	1.78	0.18	5.63
	Initial	33.11	3.0	0.35	0.096	5	1.2	11.2	2.73	0.15	2.95	0.68	60.45
200 RPM, 40 L/min	Final	<dl	0.97	0.29	0.3	1.97	0.69	0.04	0.42	0.08	1.79	<dl	6.55
	Initial	19.66	1	0.41	0.73	10.2	7.1	6.32	1.517	0.21	1.87	0.11	47.45
50 RPM, 60 L/min	Final	19.29	0.95	<dl	<dl	3.85	0.45	0.04	0.48	0.04	4.83	0.1	30.03
	Initial	32.03	1	<dl	<dl	8.68	1.85	1.26	0.85	0.089	5.17	0.16	51.08
120 RPM, 60 L/min	Final	5.25	0.97	<dl	<dl	4.69	0.95	0.21	2.06	1.16	0.99	0.095	15.39
	Initial	34.06	1	<dl	<dl	28.32	5.64	0.39	2.3	1.92	2.95	0.32	76.9

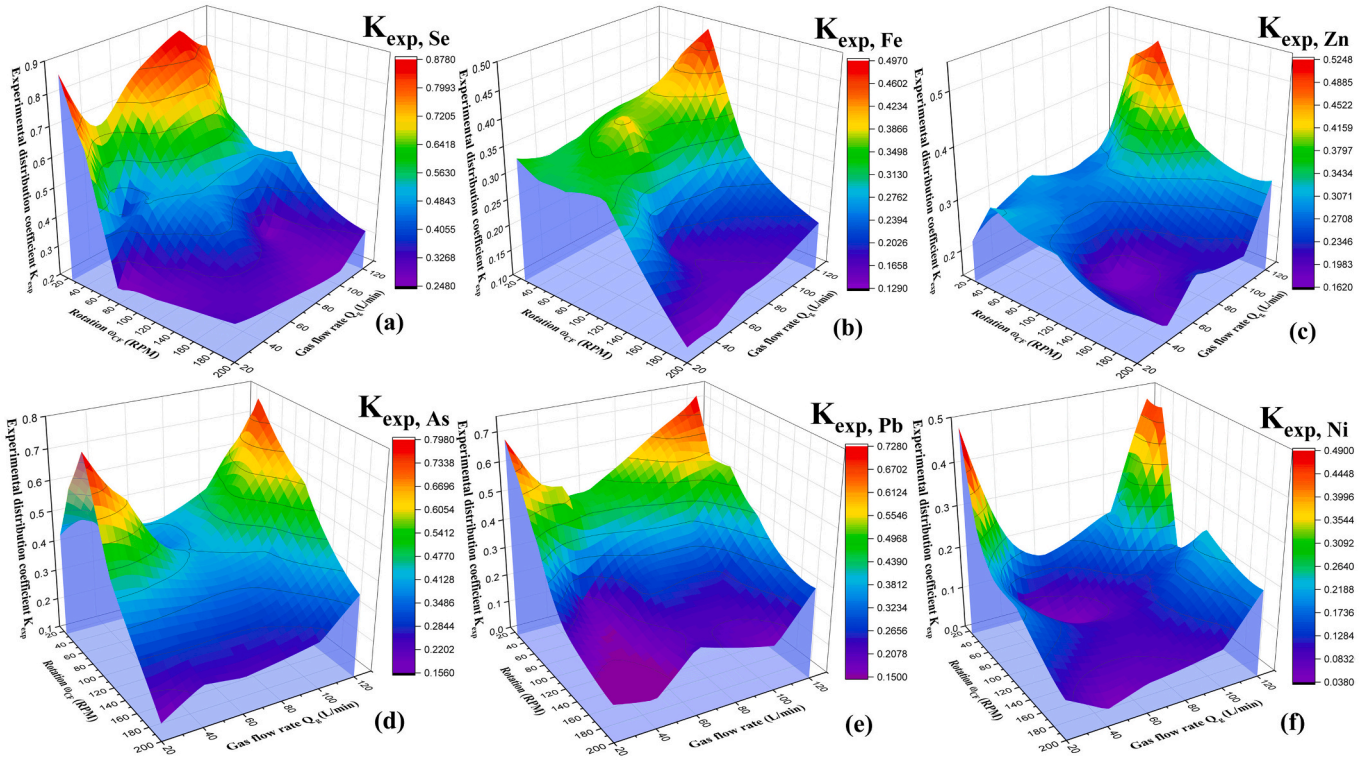

Fig. 8. Experimental distribution coefficient k_{exp} as a function of ω_{CF} and Q_g during Cooled Finger purification of tellurium: (a) Se, (b) Fe, (c) Zn, (d) As, (e) Pb and (f) Ni.

despite higher nominal purity claims by the authors [27]. In contrast, the present study evaluates overall purification performance via resulting total purity enhancement within a single fractional crystallisation step. This approach reflects the intended role of the process as a supplementary pre-purification stage rather than a replacement for zone melting. As a result, direct comparison of individual impurity removal efficiencies is therefore not appropriate.

3.3. Temperature gradient

The measured vertical temperature gradient, G_{ver}, initially reached approximately 0.16 K/mm and stabilized at around 0.06 K/mm for the remainder of the process, while the horizontal temperature gradient G_{hor} ranged between 0.4 and 4.2 K/mm (compare Fig. 9). The measurements were performed at 60 L/min without rotation and therefore represent reference condition rather than a complete mapping of the thermal field.

The reported gradients are based on temperature differences between two fixed measurement points. For assessment the solidification regime, the relevant gradient corresponds to the condition where one measurement point is located in the solid phase and the other remains in the liquid phase. This condition is achieved only in the horizontal measurement configuration (Fig. 9 (b)). At the beginning of the experiment, both thermocouples were located in the liquid phase; the transition to a solid-liquid measurement condition is indicated by the increase in the G_{hor} observed after approximately 20 min from the onset of crystallisation. From this point onward, the measured horizontal temperature gradient reflects the thermal conditions at the solid-liquid interface and can therefore be used to characterise the solidification regime according to Fig. 2.

The growth rate, V_{CF} under stationary conditions (without rotation) was approximately 0.0092–0.0094 mm/s. Under the combined conditions of G_{hor} and V_{CF} the expected solidification morphology lies within

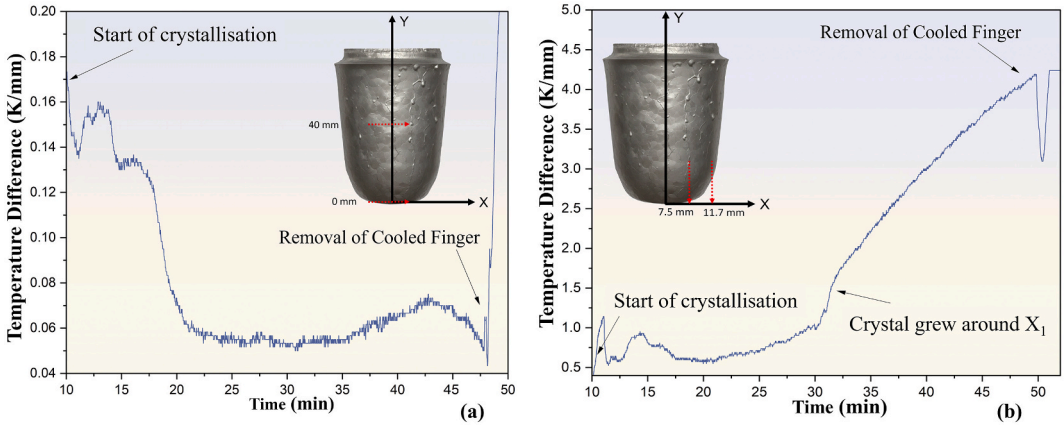

Fig. 9. Measured temperature differences during solidification: (a) vertical temperature gradient (b) horizontal temperature gradient.

the oriented cellular structures (compare Fig. 2), approaching the transition to coarse oriented dendritic growth. However, examination of the crystallised product revealed no clear evidence of dendritic features (Fig. 10(a)). Instead, the solidification morphology was dominated by oriented cellular growth in the growth direction. For clarity, the expected growth of solidification morphology is therefore illustrated in simplified form in Fig. 11. Comparing the cellular and planar growth morphologies in Fig. 2 indicates that the Cooled Finger process operates close to the planar stability limit in terms of V_{CF}, but that the available G are insufficient to fully suppress cellular instabilities [26]. From a purification processing perspective, this oriented cellular regime is preferable to dendritic solidification, as solute re-distribution occurs preferentially along the growth direction rather than being trapped between dendrite arms.

At lower Q_g, reduced heat extraction capacity of the Cooled Finger limits the attainable temperature gradient G at the solid-liquid interface, thereby weakening directional heat flow away from the interface. Under such conditions, the liquid ahead of the interface could become effectively undercooled due to solute enrichment instead of temperature, promoting dendritic instabilities rather than stabilising the cellular front. This is consistent with the observed interface morphology, where enhanced local undercooling that would lead to increased solidification rates at the interface causes the formation of equiaxed dendritic structures (Fig. 10b). In contrast, high Q_g are expected to enhance heat removal from the Cooled Finger, increasing G and extending the stability range for cellular or near-planar solidification. However, this stabilisation is only achieved provided that the solidification velocity does not increase excessively. In the present Cooled Finger setup, the parallel increase in cooling intensity and solidification velocity cannot be fully decoupled, limiting the extent to which a stable planar front can be maintained.

Rotation, which was not applied during gradient measurements, is expected to further modify both the thermal and solute fields by enhancing convective heat transfer in the melt and reducing solute boundary layer thickness δ [22]. While this may improve mass transport conditions, it simultaneously alters the local solidification dynamics, making control of the thermal and solute fields challenging. Achieving planar solidification in the Cooled Finger process therefore requires combined optimisation of cooling intensity and rotational speed.

In comparison to established techniques such as zone melting, where thermal gradients and growth conditions can be more effectively decoupled, the Cooled Finger approach exhibits inherent limitations in separating thermal control from mass transport or growth control. The results obtained in this study therefore supports that, under the investigated conditions, the Cooled Finger method is better suited as a supplementary purification step rather than a standalone technique.

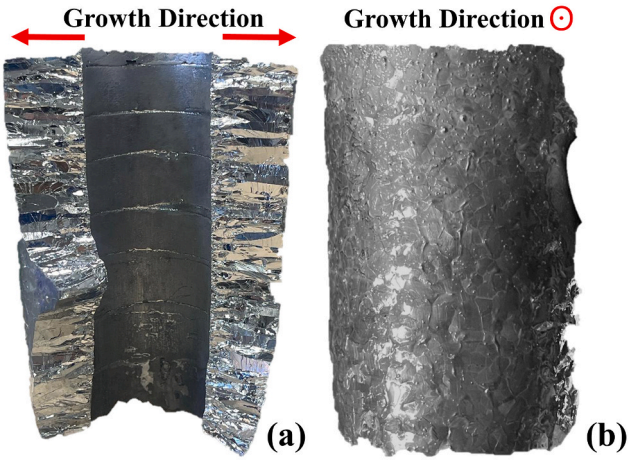

Fig. 10. Surface morphology of crystallised product (a) cross-section (b) solid-liquid interface.

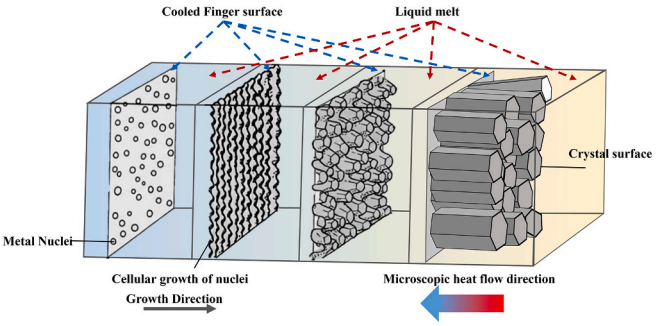

Fig. 11. Schematic illustration of the solidification morphology during Cooled Finger crystallisation, showing oriented cellular growth.

3.4. Burton-Prim-Slichter (BPS) analysis and evaluation of the diffusion boundary layer

According to the BPS model, the effective distribution coefficient $k_{eff} = k_{exp}$ is related to the ratio of diffusion boundary layer thickness to solute diffusivity $\left(\frac{\delta}{D}\right)$. Linearising the model yields a proportional relationship between $ln\left(\frac{1}{k_{exp}} - 1\right)$ and the growth rate V_{CF}, from which $\frac{\delta}{D}$ can be obtained from the slope of the fitted lines. The individual BPS plots constructed for each ω_{CF} are presented in Fig. 12 (a)-(e), while the resulting $\frac{\delta}{D}$ values are summarised in Fig. 13. Although V_{CF} and δ contribute to the effective segregation behaviour, a direct quantitative correlation between these two values cannot be established from the present data.

For Se, As and Ni, $\frac{\delta}{D}$ decreases systematically with increasing rotation rate. This behaviour is consistent with classical boundary layer theory. The observed trend therefore supports the expected dynamic thinning of δ under increasing rotational intensity, in agreement with previous studies on convection-controlled segregation in melts.

In contrast, Pb, Fe and Zn exhibit a non-monotonic dependence of $\frac{\delta}{D}$ on rotation rate. An initial increase in $\frac{\delta}{D}$ is observed between 25 and 80 RPM, followed by a decrease at higher rotational speeds. Since only a single diffusion boundary layer is present under each experimental condition, changes in $\frac{\delta}{D}$ cannot be attributed solely to melt-dynamic effects. Instead, the behaviour suggest that the effective diffusivity D of the segregating species may vary with processing conditions.

One possible explanation is the transient formation of solute complexes or compound species in the melt. If transport occurs partially through compound diffusion rather than individual elemental diffusion, the effective diffusivity may differ from the tabulated values for pure elements. Such a change would alter the extracted $\frac{\delta}{D}$ ratio without necessarily reflecting a true increase in δ. Similar considerations of compound-assisted transport during high-purity metal purification have been discussed in previous studies [29].

These results indicate that while rotation predominantly governs δ thinning [17,27,30], element-specific interactions in the melt may additionally influence the apparent diffusion behaviour. Consequently, the $\frac{\delta}{D}$ values derived from the BPS analysis should be interpreted as effective transport parameters reflecting the coupled influenced of convection and chemical interactions, rather than purely geometric boundary layer thicknesses.

4. Summary

The present study evaluated the purification behaviour of tellurium in a rotational Cooled Finger crystallisation system, with particular

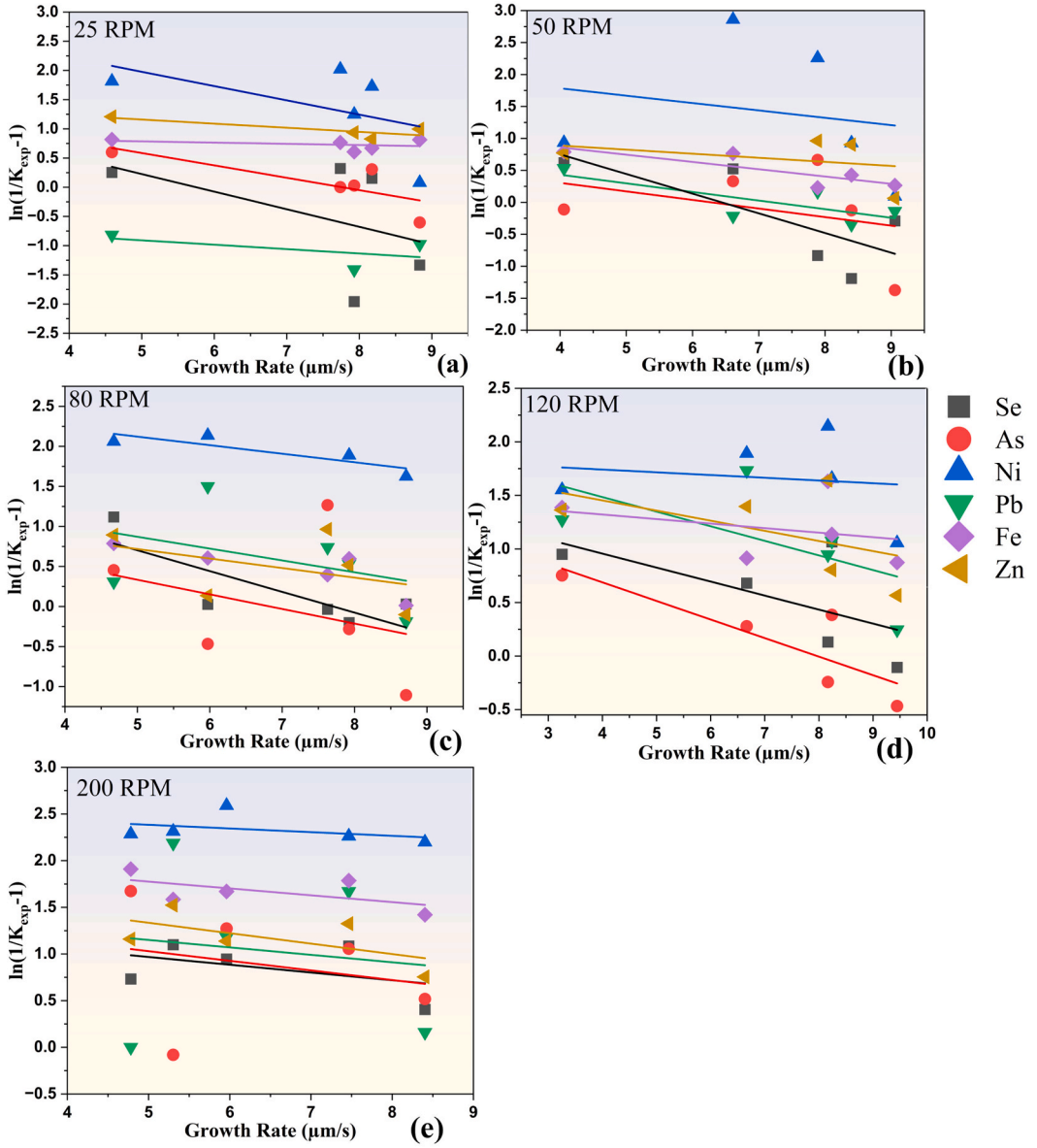

Fig. 12. Burton-Prim-Slichter model plots for ω_{CF} of (a) 25 RPM, (b)50 RPM, (c) 80 RPM, (d) 120 RPM, and (e) 200 RPM.

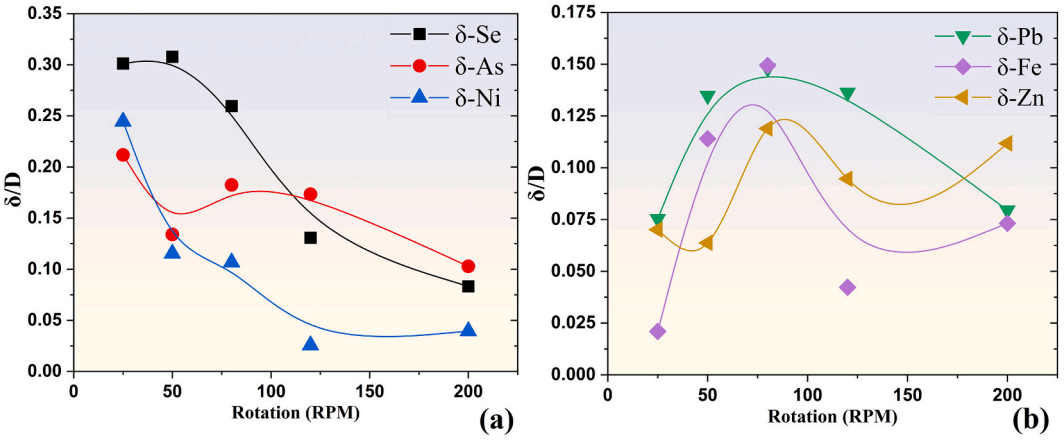

Fig. 13. Dependence of $\frac{\delta}{D}$ ratio on ω_{CF}, (a) for Se, As and Ni, and (b) for Pb, Fe and Zn.

focus As, Fe, Ni, Pb, Se, and Zn. Across the investigated parameter window, stable directional growth was maintained within the cellular solidification regime, with measured horizontal temperature gradients in the range of 0.4–4.2 K/mm and average interface velocities of approximately 9 μm/s.

Purification efficiencies between 42% and 90% were achieved within a fixed crystallisation time of 30 min, with all refined samples exceeding 4 N4 purity from 4 N and two reaching 5 N purity. A clear dependence of impurity rejection on rotational speed was observed, while cooling gas flow rate primarily influenced material yield. The yield-purity trade-off demonstrates that high rotational speeds combined with low to moderate cooling intensities provide the most favourable compromise between purification performance and material recovery.

Element-specific segregation behaviour revealed systematic trends for Se, As, and Ni, while Pb, Fe and Zn exhibited non-monotonic responses to increasing rotation. The experimental distribution coefficients k_{exp} for the investigated impurities fall within the following ranges: Se (0.25–0.87), Fe (0.13–0.50), Zn (0.16–0.52), Pb (0.15–0.73), and Ni (0.03–0.50). Analysis within the Burton-Prim-Slichter framework showed that the effective $\frac{\delta}{D}$ ratio decreases with increasing rotational speed for most elements, indicating the dynamic thinning of the solute boundary layer. Deviations from monotonic trends suggest that multi-component interactions in the melt may influence the effective transport behaviour of certain elements.

In the context of conventional zone melting, the present results highlights the potential of the Cooled Finger process as a rapid pre-purification step. While literature reports that multi-pass zone melting typically requires 10–35 h to achieve significant impurity reduction and ultra-high purity levels, the present study demonstrates that substantial impurity removal from 60 ppm to ~5 ppm can be achieved within a single 30 min crystallisation. Even under less favourable conditions, impurity levels were reduced from 51.08 ppm to 30.03 ppm within the same processing time.

Although the absolute purity levels remain below those attainable by extended multi-pass zone melting, the results proved that the Cooled Finger is highly effective in rapidly reducing the initial impurity burden, enabling more efficient downstream purification and reducing processing time required to reach ultra-high purity levels. In this context, the primary value of the process lies not in maximizing individual impurity removal, but in improving overall purification process efficiency, throughput and time-to-purity. Therefore, the technical feasibility of the Cooled Finger process at laboratory scale has been demonstrated. However, the work should be regarded as a proof-of-concept investigation, and further studies are required to evaluate industrial implementation. Future research should address scale-up considerations, including the influence of geometry on productivity, optimisation of heat extraction, and feasibility of continuous or semi-continuous operation. Further studies should also consider the behaviour of other impurity elements commonly present in copper anode slime-derived tellurium, including Bi, Sb, Sn and Ag, to further broaden the evaluation of the Cooled Finger purification process.

Author Contribution

Conceptualization, H.C.; methodology, H.C. and S.F.; software, H.C.; validation, H.C. and S.F.; formal analysis, H.C.; investigation, H.C.; resources, B.F.; data curation, H.C.; writing—original draft preparation, H.C.; writing—review and editing, S.F.; visualization, H.C.; supervision, S.F. and B.F.; project administration, S.F.; funding acquisition, B.F. All authors have read and agreed to the published version of the manuscript.

Funding

This research was funded by the Federal Ministry for Economic Affairs and Climate Action of Germany (Bundesministerium für Wirtschaft und Klimaschutz), grant number 03EN2056C.

Declaration of competing interest

The authors declare that they have no known competing financial interests or personal relationships that could have appeared to influence the work reported in this paper.

Data availability

Data will be made available on request.

References

[1] H. Chung, S. Friedrich, J. Becker, B. Friedrich, Purification principles and methodologies to produce high-purity tellurium, Can. Metall. Q. (2024) 1–17, https://doi.org/10.1080/00084433.2024.2355031.
[2] H. Zhang, et al., Advances in tellurium recovery and purification: a comprehensive review of separation methods and emerging technologies, Resour. Conserv. Recycl. 215 (2025) 108160, https://doi.org/10.1016/j.resconrec.2025.108160.
[3] Q. Tian, S. Qiao, X. Guo, Z. He, Z. Xu, D. Li, Recovery and high-purity preparation of tellurium from secondary sources—a review, J. Sustain. Metall. 11 (4) (2025) 3361–3387, https://doi.org/10.1007/s40831-025-01248-3.
[4] A.M. Hageman, et al., Purification of tellurium to 6N using a multistage vacuum distillation method, in: Penetrating Radiation Systems and Applications VIII, SPIE, 2007, p. 67070Z, https://doi.org/10.1117/12.740525.
[5] S. Ali, D. Prasad, N. Munirathnam, T. Prakash, Purification of tellurium by single-run multiple vacuum distillation technique, in: Separation and Purification Technology 43, Elsevier, Radarweg 29, 1043 NX Amsterdam, Netherlands, 2005, pp. 263–267, https://doi.org/10.1016/j.seppur.2004.11.008, 3.
[6] W.G. Pfann, Zone Melting, Science 135 (3509) (1962) 1101–1109, https://doi.org/10.1126/science.135.3509.1101.
[7] M. Shim, Y.M. Kim, H.H. Lee, S.J. Hong, J.H. Lee, Separation behavior of impurities and selenium reduction by the reactive zone refining process using high-frequency induction heating to purify Te, J. Cryst. Growth 455 (2016) 6–12, https://doi.org/10.1016/j.jcrysgro.2016.09.032.
[8] A. Zaiour, et al., Purification of tellurium to nearly 7N purity, Mater. Sci. Eng. B 131 (1–3) (2006) 54–61, https://doi.org/10.1016/j.mseb.2006.03.029.
[9] Q. Tian, Z. He, Z. Xu, D. Li, X. Guo, Experimental analysis of high purity tellurium prepared by zone refining, Metall. Mater. Trans. B Process Metall. Mater. Process. Sci. (2024), https://doi.org/10.1007/s11663-023-02989-w.
[10] N.R. Munirathnam, D.S. Prasad, J.V. Rao, T.L. Prakash, High Purity Tellurium Production Using Dry Refining Processes, 2005.
[11] N.R. Munirathnam, D.S. Prasad, C. Sudheer, A.J. Singh, T.L. Prakash, Preparation of High Purity Tellurium by Zone Refining, 2002.
[12] N.R. Munirathnam, D.S. Prasad, C. Sudheer, T.L. Prakash, Purification of tellurium to 6N + by quadruple zone refining, J. Cryst. Growth 254 (1–2) (2003) 262–266, https://doi.org/10.1016/S0022-0248(03)01141-2.
[13] D.S. Prasad, N.R. Munirathnam, J.V. Rao, T.L. Prakash, Effect of multi-pass, zone length and translation rate on impurity segregation during zone refining of tellurium, Mater. Lett. 60 (15) (2006) 1875–1879, https://doi.org/10.1016/j.matlet.2005.12.041.
[14] Shanghai Nonferrous Metals Network, Technological developments and applications of high-purity tellurium and high-purity indium (translated from Chinese), Accessed: Apr. 18, https://news.smm.cn/news/102814719, 2026.
[15] H. Shingu, K. Arai, , et al.S. A. Corporation, Process for producing high-purity aluminium, 1982. https://patents.google.com/patent/US4469512A/en.
[16] M. Gotenbruck, D.C. Curtolo, S. Friedrich, B. Friedrich, The effectiveness of cooled-finger and vacuum distillation processes in view of the removal of Fe, Si and Zn from Aluminium, Metals 12 (12) (2022) 2027, https://doi.org/10.3390/met12122027.
[17] M.J. Rodriguez-Rojas, S. Friedrich, B. Friedrich, Feasibility of employing the cooled finger, a fractional crystallization method for the purification of magnesium, J. Sustain. Metall. 8 (3) (2022) 1276–1289, https://doi.org/10.1007/s40831-022-00572-2.
[18] D.C. Curtolo, S. Friedrich, M. Noack, B. Friedrich, Numerical and experimental investigation of germanium refining via fractional crystallization, Metals 10 (973) (2020), https://doi.org/10.3390/met10070973.
[19] H. Zhang, G. Qian, J. Pang, Z. Wang, Enhancing rapid and deep removal of trace impurities from tellurium by an immersion rotational segregation purification process, Metall. Mater. Trans. B Process Metall. Mater. Process. Sci. (2024), https://doi.org/10.1007/s11663-024-03167-2.
[20] J.A. Burton, R.C. Prim, W.P. Slichter, The distribution of solute in crystals grown from the melt. Part I. Theoretical, J. Chem. Phys. 21 (11) (1953) 1987–1991, https://doi.org/10.1063/1.1698728.

[21] D. Curtolo, S. Friedrich, D. Bellin, G. Nayak, B. Friedrich, Definition of a first process window for purification of aluminum via “cooled finger” crystallization technique, Metals 7 (9) (2017) 341, https://doi.org/10.3390/met7090341.
[22] D. Curtolo, et al., Experimental and numerical investigation of a solidification-based aluminum-cooled finger refinement process from Micro to macro-scale, Metall. Mater. Trans. A 54 (10) (2023) 3988–4011, https://doi.org/10.1007/s11661-023-07147-0.
[23] M. Roumié, K. Zahraman, A. Zaiour, Y. Mohanna, M. Hage-Ali, Study of segregation process of impurities in molten tellurium after one pass of three conjoint zones in zone refining, J. Cryst. Growth 289 (1) (2006) 260–268, https://doi.org/10.1016/j.jcrysgro.2005.11.002.
[24] A. Zaiour, B. Hamdoun, Effect of temperature on segregation coefficients of impurities in tellurium, Phys. Scr. 70 (2–3) (2004) 193–196, https://doi.org/10.1088/0031-8949/70/2-3/019.
[25] Hanwen Chung, S. Friedrich, B. Friedrich, Innovative approach for producing high-purity tellurium, 2025, https://doi.org/10.13140/RG.2.2.26912.29447.
[26] W. Kurz, D.J. Fisher, Fundamentals of Solidification, Trans Tech Publ., Aedermannsdorf, 1992, p. 1989.
[27] Q. Luo, et al., Enhanced purification efficiency of high-purity tellurium via sustainable rotary crystallization: a focus on impurity migration behavior, JOM 77 (8) (2025) 6231–6244, https://doi.org/10.1007/s11837-025-07466-0.
[28] A.P. Ubelis, Temperature dependence of the saturated vapor pressure of tellurium, J. Eng. Phys. 42 (3) (1982) 309–315, https://doi.org/10.1007/BF00827754.
[29] N. Xiong, S. Friedrich, B. Friedrich, Purification of the Al2Cu intermetallic compound via zone melting crystallization technique, J. Mater. Res. Technol. 26 (2023) 973–983, https://doi.org/10.1016/j.jmrt.2023.07.199.
[30] D.C. Curtolo, M.J. Rodriguez-Rojas, S. Friedrich, B. Friedrich, Alternative fractional crystallization-based methods to produce high-purity aluminum, J. Mater. Res. Technol. 12 (2021) 796–806, https://doi.org/10.1016/j.jmrt.2021.03.025.